http://www.diva-portal.org

Postprint

This is the accepted version of a paper published in *Journal of Marine Science and Engineering*. This paper has been peer-reviewed but does not include the final publisher proof-corrections or journal pagination.

Citation for the original published paper (version of record):

Cheemakurthy, H., Barsoum, Z., Burman, M., Garme, K. (2022)
Comparison of Lightweight Structures in Bearing Impact Loads during Ice–Hull Interaction.
Journal of Marine Science and Engineering, 10(6): 794
https://doi.org/10.3390/jmse10060794

Access to the published version may require subscription.

N.B. When citing this work, cite the original published paper.

Permanent link to this version:
http://urn.kb.se/resolve?urn=urn:nbn:se:kth:diva-313910

Journal of
Marine Science and Engineering

MDPI

Article

Comparison of Lightweight Structures in Bearing Impact Loads during Ice–Hull Interaction

Harsha Cheemakurthy *, Zuheir Barsoum, Magnus Burman and Karl Garme

Department of Engineering Mechanics, KTH Royal Institute of Technology, 114 28 Stockholm, Sweden; zuheir@kth.se (Z.B.); mburman@kth.se (M.B.); garme@kth.se (K.G.)
* Correspondence: harsha@kth.se

Abstract: The current study focuses on the impact loading phase characteristic of thin first year ice in inland waterways. We investigate metal grillages, fibre reinforced plastic (FRP) composites and nature-inspired composites using LS Dyna. The impact mode is modelled as (a) simplified impact model with a rigid-body impactor and (b) an experimentally validated ice model represented by cohesive zone elements. The structural concepts are investigated parametrically for strength and stiffness using the simplified model, and an aluminium alloy grillage is analysed with the ice model. The metal–FRP composite was found to be the most favourable concept that offered impact protection as well as being light weight. By weight, FRP composites with a Bouligand ply arrangement were the most favourable but prone to impact damage. Further, aluminium grillage was found to be a significant contender for a range of ice impact velocities. While the ice model is experimentally validated, a drawback of the simplified model is the lack of experimental data. We overcame this by limiting the scope to low velocity impact and investigating only relative structural performance. By doing so, the study identifies significant parameters and parametric trends along with material differences for all structural concepts. The outcomes result in the creation of a viable pool of lightweight variants that fulfil the impact loading phase. Together with outcomes from quasi-static loading phase, it is possible to develop a lightweight ice-going hull concept.

Keywords: composites; metal grillage; aluminium hull; ice loads; LS Dyna; urban waterborne mobility; inland waterways; impact modelling; bio-inspired structures; ice-going hull

check for updates

Citation: Cheemakurthy, H.; Barsoum, Z.; Burman, M.; Garme, K. Comparison of Lightweight Structures in Bearing Impact Loads during Ice–Hull Interaction. *J. Mar. Sci. Eng.* **2022**, *10*, 794. https://doi.org/10.3390/jmse10060794

Academic Editors: Murat Ozdemir, Selda Oterkus and Erkan Oterkus

Received: 27 April 2022
Accepted: 6 June 2022
Published: 9 June 2022

Publisher's Note: MDPI stays neutral with regard to jurisdictional claims in published maps and institutional affiliations.

Copyright: © 2022 by the authors. Licensee MDPI, Basel, Switzerland. This article is an open access article distributed under the terms and conditions of the Creative Commons Attribution (CC BY) license (https://creativecommons.org/licenses/by/4.0/).

1. Introduction

Inland waterborne navigation in ice is important from an economic and mobility perspective. Robust lightweight hulls would lower fuel consumption and increase payload capacity. The contemporary, state-of-the-art design of ice-class vessels recommends steel [1–3] and the knowledge gap is the absence of viable lightweight hulls in practice. In a previous study, lightweight structures against quasi-static ice pressure loading [4] were investigated. In this study we investigate ice impact loading.

During ice–hull interactions, one typically observes low speed impact loading. Several such experimental and numerical studies have used steel impactors to study structural response [5,6]. Recent studies have been performed using ice impactors [7–11]. However, the complex nature of ice and a lack of analytical models [12] makes it difficult to generalise structural response. This establishes the need for experimental studies for new routes due to difference in ice properties [13]. In the current study, the target operational zone is freshwater inland waterways found in Lake Mälaren, Sweden, for which ice impact experimental data are available from TUHH Hamburg [11,14].

Regarding the assessment of lightweight structures in the literature, Herrnring and Kubiczek [11] performed ice drop tests on an aluminium grillage and observed structural integrity however with some plastic deformations. Crum and McMichael [15] observed good impact resistance for aluminium alloy based naval vessels. Within composites, a

study by Wu and Li [16] on aluminium-honeycomb sandwich panels and impact with ice showed no catastrophic failure. Burman and Niclasen [14] studied the ice impact behaviour on sandwich panels in a preliminary study. Niclasen [17] developed a methodology for ice impact experimental setup of glass-fibre reinforced plastic and carbon-fibre reinforced plastic (CFRP) sandwich panels. Banik and Zhang [10] studied the low speed impact of ice on CFRP sandwich composites and noted negligible damage with thicker face sheets. However, FRPs might not be the best alternative since they are prone to barely visible impact damage (BVID) that can cause significant loss in residual strength [5,18,19].

To expand our pool of promising impact resilient structural concepts, we turn to nature for inspiration. The study of woodpecker's drumming motion revealed a composite structure consisting of hard, porous and viscoelastic layers in the head and beak, which results in impact toughness and light weight [20]. Bighorn sheep's horns were found to be a composite of tough and stiff materials, resulting in high energy impact resilience albeit causing high weight [21]. The study noted the advantage of a tapered spiral geometry in shock mitigation and damage resistance, which were also observed in the clubs of stomatopods and beetle hind wings that had a Bouligand helical structural arrangement [22,23].

In Cheemakurthy and Barsoum [4], a tri-layer hull structural concept, consisting of abrasion resistant, impact resistant and quasi-static pressure resistant layers, was introduced. The current study focuses on finding candidates for the impact resistant layer, where five concepts—metal grillages, FRP composites (Bouligand and conventional), metal–FRP composites and two bio-inspired composites are parametrically explored in LS Dyna 4.7.7. Two impact models are applied—(a) steel impactor model to compare the relative impact performance of structural concepts and (b) an experimentally validated cohesive zone method (CZM) ice model to study a particular case of an aluminium grillage.

The study identifies lightweight candidates, significant parameters and their trends with respect to structural performance for each concept. Further, it shows the survivability of an aluminium hull under impact loading. Other parametric studies in the literature include the investigation of weight and cost of composite ship structures [24], low speed impacts on composites [25] and parametric optimization of composites plates [26]. In contrast, the current study explores a greater number of parameters and includes novel composite arrangements and metal grillages.

2. Concept for Lightweight Hull Structure and Candidates

Ice–hull interaction is considered stochastic due to its dependence on local ice properties and the complex nature of ice, resulting in an absence of physical models [12,27]. By assuming thin first-year ice and proper route planning, we can limit the stochasticity and focus on (a) advancement in level ice, (b) small ice floe collision and (c) brash ice operations. Among these, we observe short-interval dynamic forces during initial impact, initiation of ice fracturing, spalling and the extrusion of material [28].

For the tri-layer structural concept introduced in Cheemakurthy and Barsoum [4], five structural concepts that fulfil the impact resistant layer are chosen. Their representations and relative masses are shown in Figure 1. Metal grillages represent the current state-of-the-art, FRP composites have been explored in the literature, metal–FRP composites are explored considering the BVID susceptibility of FRP composites, helically arranged Bouligand composites, stiff–tough and stiff–viscoelastic–tough composites are explored as bio-inspired candidates. Their geometric parametrization is based on structural design calculations, rule-based design and practical aspects. These are compiled in Table 1 with respective material properties in Table 2.

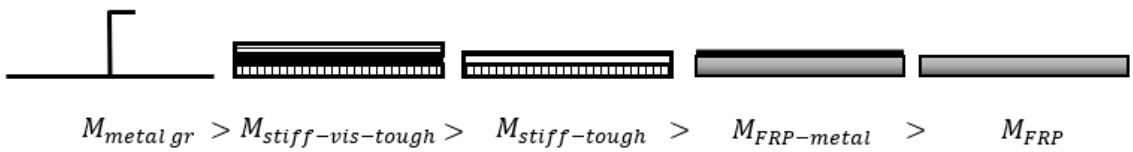

Figure 1. Five structural concepts that will be investigated arranged according to their mass.

Table 1. Structural candidates and their parametrization. The term 'ice stringer / ice stiffener' refer to members that are directly present underneath the impact location.

Structural Concept	Structural Element	Variants	Motivation
Metal Grillage	Plate thickness Stiffener spacing Stringer spacing Ice stringer/stiffener Stiffener elastic section modulus Stringer elastic section modulus Materials	10, 15, 20 mm 0.25, 0.5, 0.67 m 0.5, 0.67, 1 m Yes, No 18.4, 57.3, 94.8 cm^3 150, 303, 443 cm^3 Steel, Aluminium	Steel: State of the art [1] Aluminium: Applications in naval vessels in extreme conditions [15], ice impact survivability [9,11].
Bouligand FRP Composite	Single ply thickness Pitch angles Number of face sheets Face materials	0.3, 0.5, 0.7 mm 10°–20°, 25°, 30° 48 C-UD 235/395, C-woven 395, E-glass	Naturally occurring helical arrangement shows high impact resistance [22,23]
Conventional FRP composite	Single ply thickness Ply orientation Number of face sheets Face materials	0.3, 0.5, 0.7 mm $[+45/-45]_8$; $[+90/0]_8$; $[90/0/45/-45]_s$ 48 C-UD 235/395, C-woven 395, E-glass	Application in naval ship hulls prone to extreme working conditions [29] Ice impact survivability [10]
Stiff–Tough composite	Total plate thickness Stiff: Tough thickness ratio Stiff plate material Tough plate material Plate orientation	20, 30, 40, 50 mm 4:1, 2:1, 1:1, 1:2, 1:4 SiC, BC Steel, Aluminium Stiff-Tough; Tough-Stiff	Study of big sheep horn structure [21]. Good impact resistance
Metal–FRP composite	Face ply thickness Metal thickness Face material Metal material Ply orientation	0.3, 0.5, 0.7 mm 5, 10, 15 mm C-UD/Woven 395, E-glass Steel, Titanium alloy Bouligand; Conventional	Civil engineering applications [30] Marine propeller applications [31] Blast resistant applications [32]
Viscoelastic–tough–stiff composite	Viscoelastic layer thickness Viscoelastic layer material Tough layer thickness Tough layer material Stiff layer thickness Stiff layer material Plate orientation	0.01, 0.02 m Chloroprene rubber 0.01 m Steel 6 mm to 14 mm SiC, BC Ceramic-rubber-metal, Rubber-ceramic-metal	The study of shock resistant woodpecker drumming motion [20]

Two metal grillages of structural steel and aluminium alloy are explored. The upper parametric level corresponds to ice class rules for class 1B following Finnish Swedish Ice Class rules (FSICR) [1] for a steel barge. The lower limit corresponds to DNV-GL [33] rules for inland navigation vessels. For FRP composites, conventional and Bouligand ply arrangements are explored. Bouligand ply arrangements are achieved by placing plies having their orientations in a helical fashion at different pitch angles. The pitch angle range is inspired from literature [34]. Carbon fibre, glass fibre, uni-directional (UD) and woven fabrics are investigated. The parametric range for the conventional ply arrangement is deduced using constant stiffness design method [35] where a quasi-static rule-based ice pressure patch [1] is assumed on a FRP panel of dimensions 2.4 m $\times$ 2.4 m. The panel is optimized using a gradient-based approach using finite difference method [36] while minimizing the panel weight with constraints for stiffness compliance $\frac{w}{b} \leq 0.02$ and strength compliance $\sigma_{f,max} = \frac{E_f}{64}$ [2]. For metal–FRP composites, naturally stiff metals—steel and titanium alloys—are paired with FRP configurations. The metal sheet thickness range is increased starting from a corrosion allowable thickness. For stiff–tough composites, the stiff layer is represented by ceramics (Silicon Carbide, SiC and Boron Carbide, BC) and tough layer by metals (Aluminium alloy and structural steel). The thickness of the layers correspond to rule-based [2] plate thickness values for metals, limited to 50 mm due to practical reasons. For stiff–viscoelastic–tough composites, chloroprene rubber is chosen as the viscoelastic layer. The parametric range of rubber thickness has an upper limit 20 mm out of practical reasons.

Table 2. Properties of materials used in the parametrisation of structural candidates (unless stated specifically, the data were sourced from the engineering database in the ANSYS library [37]).

Material	Density (kg/m^3)	Young's Modulus (MPa)	Shear Modulus (MPa)	Tensile/Shear * Yield Strength (MPa)	Tensile Ultimate Strength (MPa)	Orthotropic Strain Limit
Structural Steel	7850	2×10^5	7.69×10^4	250	460	
Aluminium alloy	2770	7.1×10^4	2.67×10^4	280	310	
Titanium alloy	4419	Steinberg Guinan Strength		920	2120	Material model: [38]
Carbon fibre 230	1490	X: 1.21×10^5 Y, Z: 8600	XY, XZ: 4700 YZ: 3100	X: 2231 Y, Z: 29		Y, Z: 0.0032 X: 0.0167
Carbon fibre 395	1540	X: 2.09×10^5 Y, Z: 9450	XY, XZ: 5500 YZ: 3900	X: 1979 Y, Z: 26		Y, Z: 0.0031 X: 0.0092
E-glass	2000	X: 4.5×10^4 Y, Z: 1×10^4	XY, XZ: 5000 YZ: 3846.2	X: 1100 Y, Z: 35		Y, Z: 0.0035 X: 0.0244
Boron carbide	2516	1.25×10^4 *	1.99×10^5	1180	Johnson Holmqvist Strength continuous, material model: [39]	
Silicon carbide	3215	1.17×10^4 *	1.93×10^5	1300	ANSYS Engineering database	
Vulcanized Chloroprene rubber	1000	ANSYS Engineering database			Ogden 3rd order Material model: [40]	

* Hugoniot Elastic limit.

3. Finite Element Method (FEM) Modelling

It is assumed that ice floes impact the bow region of a barge, such that the bow surface normal is parallel to the ice velocity vector. This makes the approach conservative. A simplified impact model is adopted in order to perform the parametric study. The model uses a rigid body impactor, resulting in ~10–15 times higher computational efficiency. Next, we use an experimentally validated ice representative impact model using CZM elements to study the performance of aluminium grillage. The investigative methodology is described in Figure 2. The simplified impact model gives comparative insights, while the refined model provides an understanding of structural performance.

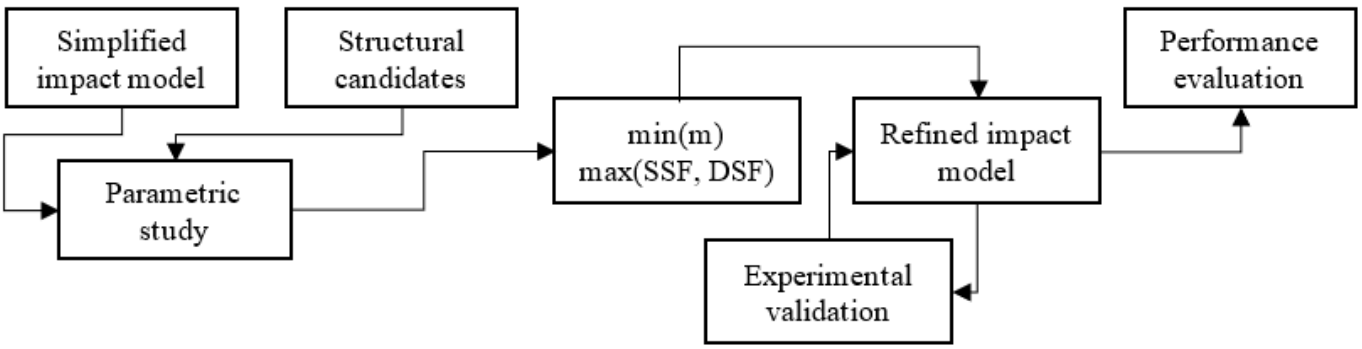

Figure 2. Investigative methodology for studying ice impact.

3.1. Simplified Impact Model

The rigid body impactor must be a good substitute to the ice model. Correspondingly, the impactor dimensions is deduced, so that the mean impact pressure is equal to the largest freshwater ice crushing strength of 38 MPa observed during bore-hole tests [41], since the crushing strength represents the maximum possible ice pressure for a structure [42]. For a design vessel speed of 6 knots, the contact area corresponding to the high pressure zone (HPZ) area [43] and the length and mass of the impactor are calculated (see Table 3).

Table 3. Geometry details of impactor.

Parameter	Value	Geometry
Radius of circular portion	56 mm	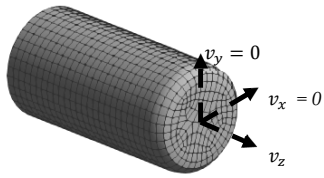
Area of impact	~0.01 m^2 [44]	
Length of impactor	0.3 m	
Mass	42.4 kg	
Mean impact stress	~40 MPa	
Speed (x, y, z)	(0, 0, 6) knots	

3.2. Refined Impact Model

The refined impact model uses CZM, which have been previously used in studies to simulate brittle ice [45–48]. Here, we use Herrnring and Kellner [48]'s approach in designing the ice model. The method works on the principle of the traction–separation law (TSL), where the traction between cohesive elements is dependent on their intermittent distance and the elements fail upon reaching a critical value. Brittle behaviour is modelled by using a binary TSL, such that all inelastic deformation corresponds to the formation of cracks. This is done by using MAT_138, laminated composites material model [49]. Element separation (delamination) is represented by compressive and tensile failure criteria as

$$\sqrt{\left(\frac{\sigma_z}{T}\right)^2 + \left(\frac{\tau_{xz}}{S}\right)^2 + \left(\frac{\tau_{yz}}{S}\right)^2} = 1; \quad \sigma_z > 0 \tag{1}$$

$$\sqrt{\left(\frac{\tau_{xz}}{S}\right)^2 + \left(\frac{\tau_{yz}}{S}\right)^2} = 1; \quad \sigma_z \leq 0 \tag{2}$$

where T and S are the maximum traction force over which the elements sustain damage. Then, delamination is governed by the interaction of energy release rates as

$$\left(\frac{G_I}{G_{Ic}}\right)^\alpha + \left(\frac{G_{II}}{G_{IIc}}\right)^\alpha = 1 \tag{3}$$

In between bulk elements, zero-thickness cohesive elements are introduced to simulate initiation and propagation of cracks (see Figure 3). To compensate for the excessive mass from cohesive elements, the density of the solid elements is modified as

$$\rho_s' = (1 - f_m)\rho_{real} \tag{4}$$

where f_m is the mass ratio between cohesive and solid elements and ρ_{real} is the density of ice. We also increase the stiffness of the of the solid elements to compensate for artificial compliance [50]. The adapted elastic modulus of the solid elements is

$$\lim n_s \to \infty : E_s' = E_s\left(1 - \frac{1}{f_k}\right)^{-1} \tag{5}$$

The elastic modulus for the CZM elements is represented as

$$E_{CZ} = \frac{f_k t_{CZ} E_S}{0.5 L_S} \tag{6}$$

A value of stiffness ratio f_k = 10 is chosen to balance computational time with accuracy [48]. For modelling realistic fracture behaviour, the cohesive zone length for brittle fracture [51] is

$$l_{CZ} = \frac{9\pi}{32}\left(\frac{E}{1 - v^2}\right)\left(\frac{G}{\tau_{max}^2}\right) \tag{7}$$

The length l_{CZ} must capture 2–10 elements depending on the separation mode. In this model, the average element edge length was 10 mm. Tetrahedron elements were used to

ensure arbitrary crack propagation. Bulk ice is represented by element type 13 and cohesive elements are represented by type 19. The FE model is shown in Figure 3.

The mass of the ice impactor is calculated assuming a collision between the hull and a floating ice floe. Then, the ice floe weighs between 100–250 kg, assuming a floe thickness of 0.25 m (load height in FSICR ice class 1B [52]), floe wedge angle between 60–120 degrees [53] and floe diameter based on the expected breaking length L_B, defined by Lindquist [54] as

$$L_B = \frac{1}{3}L_c = \frac{1}{3}\sqrt[4]{\frac{EH^3}{12(1-\mu^2)\rho_w g}} = 1.79 \text{ m} \tag{8}$$

where L_C is the characteristic length, E is ice elastic modulus, H is the ice thickness, μ is the ice Poisson ratio, ρ_w is the freshwater density and g is the standard gravity. Table 4 shows the impactor's dimensions.

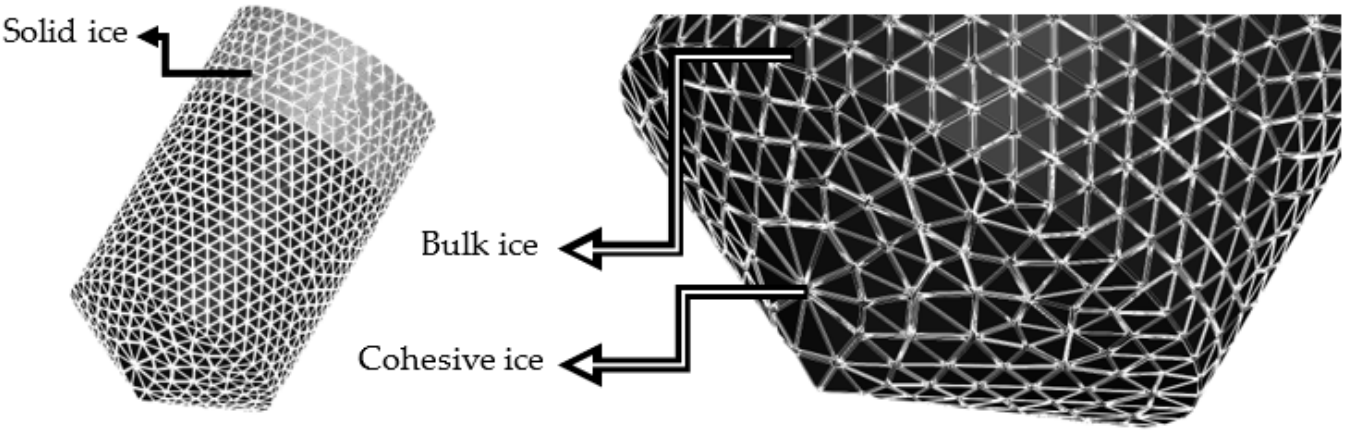

Figure 3. CZM model of ice projectile. Bulk elements are shown in dark and cohesive elements in light.

Table 4. Geometry of ice projectile.

Overall Geometry	Value
Diameter	203 mm
Height	350 mm
Mass	224 kg
Cone angle	30 degrees

3.3. Hull Panel Modeling

The hull panel under investigation is a 2.4 m × 2.4 m panel in the bow region of an inland navigation barge (see Figure 4). The projectile is placed 1 mm from the impact region at the start of the simulation. A central 'region of interest' is outlined to omit structural behaviour observed at boundaries [55]. The panel is assumed to be flat and longitudinally framed. The boundary conditions follow DNVGL [2] recommendations and are set $u_y = u_z = u_x = 0$; $r_x = 0$, while u_x, r_y and r_z are free.

3.4. Geometry, Meshing and Element Type

The geometry and meshing were carried out in ANSYS [37], while simulations were performed using an LS-Dyna solver version 4.7.7 (ANSYS, Canonsburg, USA) (see Figure 5). The meshing controls were set to have a minimum elemental quality of 0.25. The reported aspect ratios were largely under 10 and the Jacobian ratios under 3. A mesh convergence study with an element edge length of 5, 4, 3, 2.5, 2, 1.5, 1 and 0.5 mm in the impact region was performed and 1 mm was chosen to maximize computational efficiency and maintain reasonable prediction accuracy.

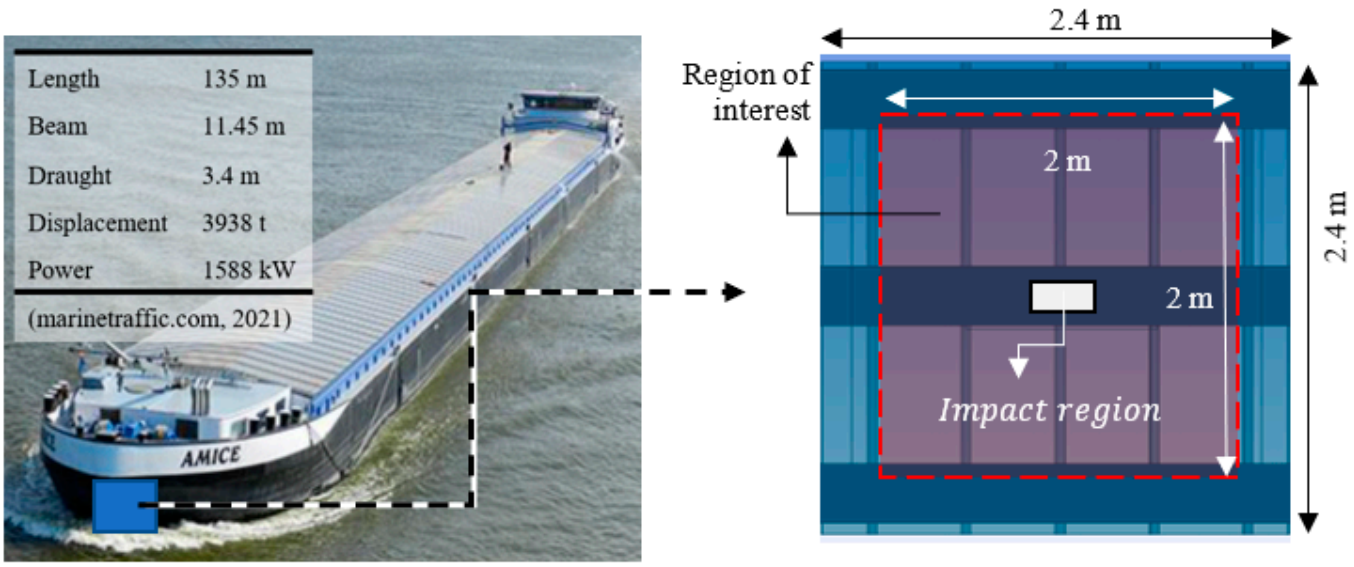

(**a**) (**b**)

Figure 4. (**a**) An inland navigation barge called 'Amice' is used as basis to develop a reference hull plate shown in (**b**).

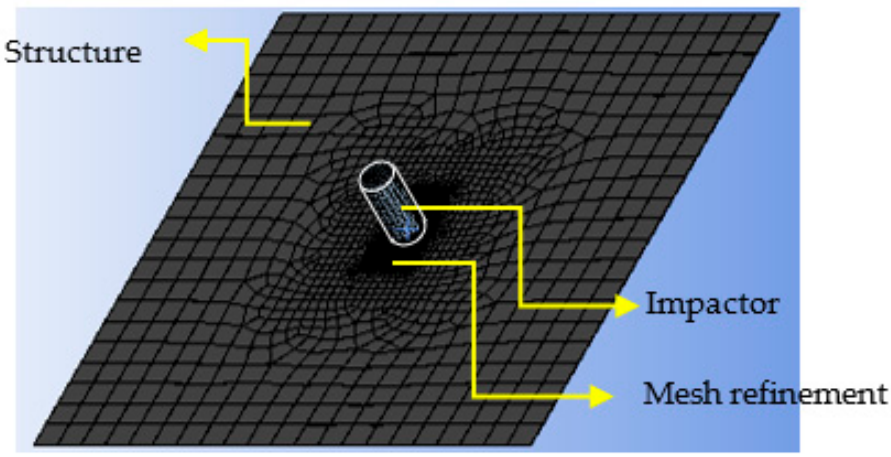

Figure 5. Panel mesh arrangement with impactor.

3.4.1. Metal Grillage

There are three structural parts in the metal grillage—plate, stiffeners, and girders. The girders have a T cross-section while the stiffeners have an L cross-section. Two types of solid elements were used: 10-node Tetrahedrons and 20-node Hexahedrons. Mesh refinements were added for the central girder, stiffeners and impact area. We use constant stress solid elements and material model MAT_003 suited for modelling isotropic and kinematic hardening plasticity.

3.4.2. FRP Composite

4-node shell elements were chosen to represent the faces instead of 8-node solid elements to save computational time as observed in other literature studies [25,56]. The material model was chosen as MAT_54 to represent composite damage [57]. The model captures the progressive degradation of ply elastic properties. The analysis settings were set to non-linear, and strain rate effects were not considered.

3.4.3. Metal–FRP Composite

A metal sheet was modelled over the FRP composite, so that the metal is represented by solid elements and FRP as shell elements with respective material models.

3.4.4. Stiff–Tough Composite

The ceramic is represented by the JH-2 model [58], which includes a criterion for erosion based on effective plastic strain and tensile failure. The material parameters were obtained from the literature [59,60], and ANSYS [37] material database 10-node Tetrahedral solid elements was used.

3.4.5. Viscoelastic–Stiff–Tough Composite

The material model MAT_183 representing a modified Ogden model suitable for neo-Hookean hyper-elastic materials was used [61,62]. A number of 10-node Tetrahedron solid elements were used.

3.5. FEA Model Validation

Based on the ice drop tests by Herrnring and Kubiczek [11] on an aluminium plate (Figure 6a), the evolution of contact force between experiments and simulations is compared. From Figure 6b, a good qualitative agreement is observed. The contact force was limited by plastic plate deformations and the peak force was 27 kN as compared to 23 kN as observed during experiments. No ice splintering and very few eroded cohesive elements at the contact surface were observed, in agreement with experimental observations.

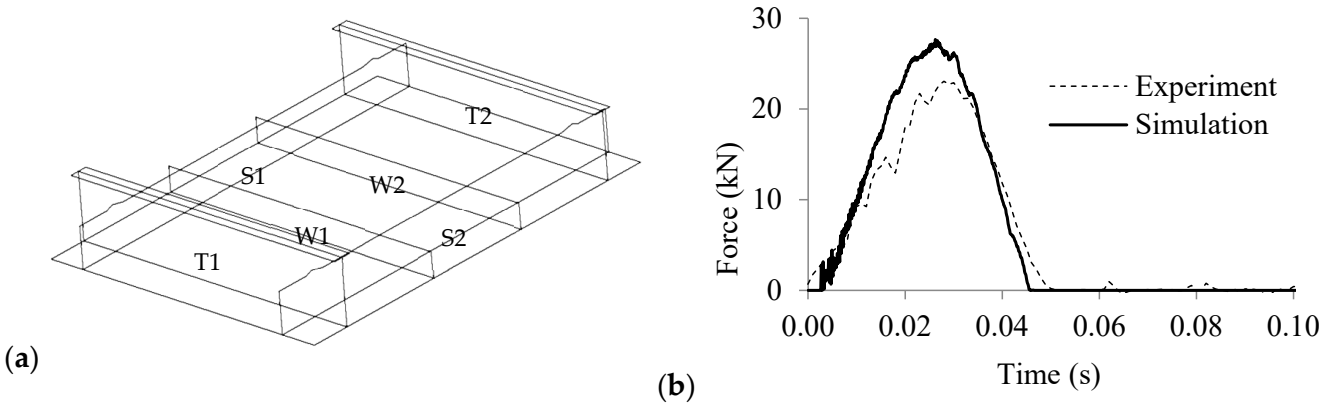

Figure 6. Comparison of experimental and FEM results. (**a**) The plate consists of two girders (T_{1-2}), two stiffeners (S_{1-2}) and two web frames (W_{1-2}), (**b**) force–time evolution chart.

4. Damage Characterization

For metal grillages, we considered the elastic region of stress–strain curve and followed the limiting rules defined by DNVGL [2] for strength and stiffness in Table 5. The lower bound for stress indicates a high degree of utilisation.

Table 5. Criteria for successful candidates.

Criteria	Limit
Peak v-m stress	70–90% of yield stress
Maximum displacement	0.02 × panel width
Element Erosion controls	Material and geometric strain limits

For metal grillages, SpW and DpW compare the strength and stiffness capacity with respect to mass of the variants [4]. Only successful candidates have a positive value, expressed as

$$SpW = \frac{(SSF - 1)}{m} \times 1000 \tag{9}$$

$$DpW = \frac{(\Delta_a/\Delta_r - 1)}{m} \times 1000 \tag{10}$$

where SpW is the strength per mass rating, DpW is the stiffness per mass rating, SSF is the stress safety factor, m is the geometric mass, Δ_a is the allowable deformation and Δ_r is the observed deformation.

For composites, we relied on defining custom failure models suitable for dynamic analyses [63]. The criterion for delamination is given by

$$\left(\frac{\max(0, \sigma_n)}{NFLS}\right)^2 + \left(\frac{\sigma_s}{SFLS}\right)^2 \geq 1 \tag{11}$$

where σ_n and σ_s are normal and shear stresses and $NFLS$ and $SFLS$ are normal and shear strengths, respectively. Beaumont [64] gives a framework for work associated micro mechanical fracture processes. Debonding is expressed as

$$W_d = \frac{\pi d^2 \sigma_r^2 l_d}{24 E_f} \tag{12}$$

where σ_f is the fibre tensile strength, d is the fibre diameter, l_d is the length of debonded zone and E_f is the fibre modulus. The fibre pull-out failure is defined as

$$W_p \leq \frac{\pi d \sigma_s l_c^2}{24} \tag{13}$$

where $l_c = \sigma_f d/2\tau$ is the critical transfer length. The strain failure criterion is set as

$$\varepsilon \leq \varepsilon_{erosion} \tag{14}$$

where $\varepsilon_{erosion}$ is the value at which the composite loses its stiffness, and the corresponding elements are omitted from the ongoing analysis. Here the value ranges between 0.03 for glass fibre and 0.04 for carbon fibre [63].

We incorporated the Hashin failure criteria [65] to incorporate damage modes, given by

Tensile fibre failure $(\sigma_{11} \geq 1)$

$$\left(\frac{\sigma_{11}}{X_T}\right)^2 + \frac{\sigma_{12}^2 + \sigma_{13}^2}{S_{12}^2} < 1 \tag{15}$$

Compressive fibre failure $(\sigma_{11} < 1)$

$$\left(\frac{\sigma_{11}}{X_C}\right)^2 < 1 \tag{16}$$

Tensile matrix failure $(\sigma_{22} + \sigma_{33} > 0)$,

$$\frac{\sigma_{22}^2 + \sigma_{33}^2}{Y_T^2} + \frac{\sigma_{23}^2 - \sigma_{22}\sigma_{33}}{S_{23}^2} + \frac{\sigma_{12}^2 + \sigma_{13}^2}{S_{12}^2} < 1 \tag{17}$$

Compressive matrix failure $(\sigma_{22} + \sigma_{33} < 0)$

$$\left[\left(\frac{Y_C}{2S_{23}}\right)^2 - 1\right]\left(\frac{\sigma_{22} + \sigma_{33}}{Y_C}\right) + \frac{(\sigma_{22} + \sigma_{33})^2}{4S_{23}^2} + \frac{\sigma_{23}^2 - \sigma_{22}\sigma_{33}}{S_{23}^2} + \frac{\sigma_{12}^2 + \sigma_{13}^2}{S_{12}^2} < 1 \tag{18}$$

Interlaminar tensile failure ($\sigma_{33} > 0$)

$$\left(\frac{\sigma_{33}}{Z_T}\right)^2 < 1 \tag{19}$$

Interlaminar tensile failure ($\sigma_{33} < 0$)

$$\left(\frac{\sigma_{33}}{Z_C}\right)^2 < 1 \tag{20}$$

SpW for composites is expressed as

$$SpW = \frac{\left(\frac{1}{IRF^z} - 1\right)}{m} \times 1000 \tag{21}$$

where IRF is the inverse reserve factor corresponding to the failure criteria Z and m is the structural mass. $SpW < 1$ indicates a high degree of utilisation.

The damage response of ceramics is a complex phenomenon, and the material deforms inelastically on impact due to microcracking, leading to fracture. A constitutive model developed by Rajendran and Kroupa [66] and built upon the Taylor [67] model defines the yield strength as

$$Y = Y_s(1 + Bln\epsilon)(1 - D) \tag{22}$$

where Y_s is the static yield strength, B is the strain rate sensitivity parameter, ϵ is the equivalent plastic strain rate and D is the damage given by

$$= \frac{16}{9}\left(\frac{1 - \overline{v}^2}{1 - 2\overline{v}}\right)C_d \tag{23}$$

where $\overline{v}$ represents the degraded elastic moduli of cracked ceramic [68] and C_d is the crack density parameter.

5. Results

In this section, we first perform an overall relative comparison of concepts and identify best variants. Next, we identify significant parameters, discuss implications and observe parametric trends. The chapter concludes with the results from the refined CZM impact model and comparison with the simplified model.

5.1. Overall Comparison

Figure 7 compares the stress capacities (SSF) of the 5 structural concepts. The FRP composite panels are the lightest (~120 kg) with SSF ranging between 1–4. Among FRP composites, Bouligand ply arrangements (red) have a slight edge over conventional ply arrangement (black). The aluminium alloy grillage (yellow) is the next lightest option (~240 kg). The next most favourable option is the metal–FRP composite (blue). The lightest variant is ~2 times heavier than the best FRP variant with approximately 20% higher stress capacity. Among metal–ceramic composites (orange), none of the variants meet the stress requirements. The addition of a viscoelastic material (brown) showed a noticeable improvement in the stress capacity through shock mitigation [20]. The heaviest of all concepts is the structural steel metal grillage.

In Figure 8, we compare the maximum deformations (DSF) for the five structural concepts. In terms of weight, both Bouligand (red) and conventional FRP (black) show similar performance. The aluminium grillage (yellow) also shows good performance, followed by the metal–FRP composite (blue). The metal–ceramic composites (orange) are inadequate in meeting the deformation requirements by a small margin. These variants in

combination with the viscoelastic layer perform the worst in terms of deformations. The steel grillage is the stiffest and the heaviest concept.

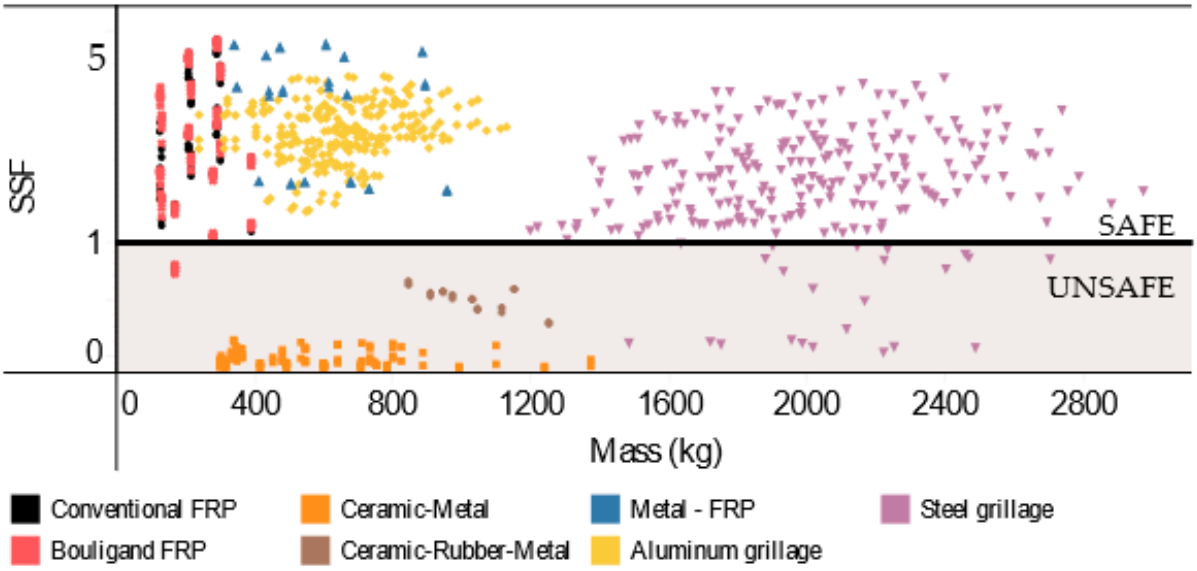

Figure 7. Comparison of stress safety factor of structural concepts with mass (*Y* axis is in log scale).

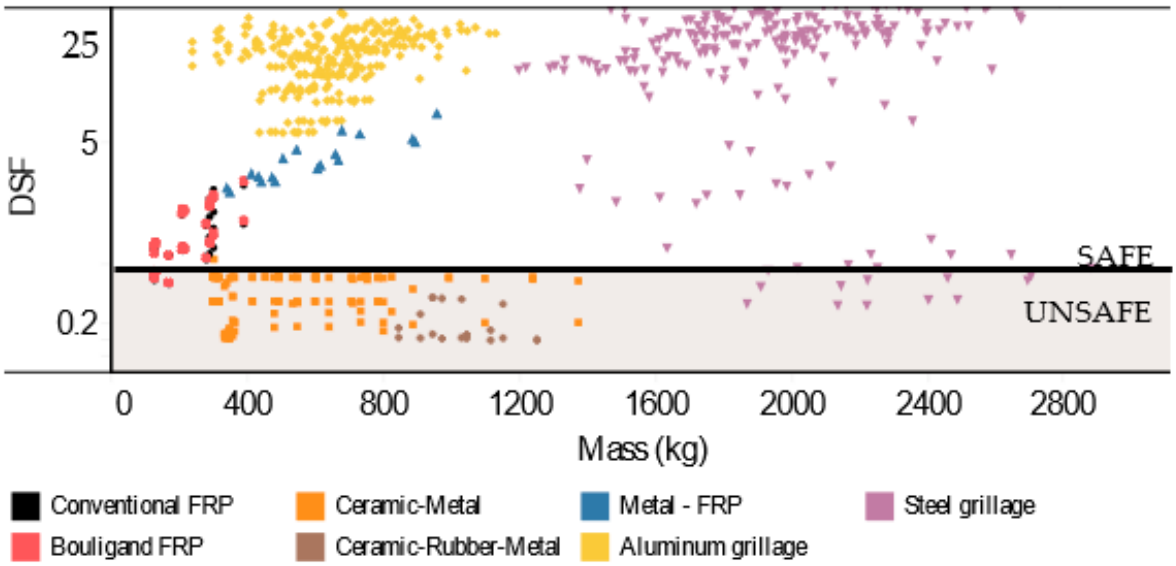

Figure 8. Comparison of structural concepts for deformation safety factor with mass.

From Figures 7 and 8 we see that SSF is a more critical factor, since its safe range is smaller than DSF. Correspondingly, we focus on strength as the limiting criteria here onwards.

Table 6 identifies the best parametric variants for all successful structural concepts against SSF. In comparing Bouligand and conventional FRPs, we see that the former has higher *SSF* and *SpW* for the same mass. However, within the metal–FRP composite, the conventional ply arrangement has a slight edge. While FRP options seem appealing due to higher *SSF* and *SpW* values, they are susceptible to punctures [69] and BVID [18]. In this case the metal–FRP composite could offer better safety along with a low mass.

Table 6. Best parametric combinations by material in terms of SSF, SpW and mass.

Structural Concept	Material	Stiffener Span (m)	Stringer Span (m)	Plate Thickness (mm)	Stiffener Z (cm^3)	Stringer Z (cm^3)	SpW (MPa/kg)	SSF (>1.1)	Mass (kg)
Metal Grillage	Al alloy	0.67	1	10	18	150	4.6	2.7	374
	St. Steel	0.67	1	10	18	150	0.118	1.14	1195
Conventional FRP	C230UD	-	0.3	C *	-		18.6	3.3	123
	C395UD	-	0.3	C *	-		13.8	2.7	127
	C395W	-	0.3	C *	-		18	3.2	122
	E-Glass	-	0.3	A **	-		2.5	1.4	165
Bouligand FRP	C230UD	-	0.3	B ***-20	-		19.7	3.4	123
	C395UD	-	0.3	B ***-20	-		14.2	2.8	127
	C395W	-	0.3	B ***-22	-		18.5	3.3	122
	E-Glass	-	0.3	B ***-20/30	-		2.7	1.44	165
Metal-FRP Composite	C395UD	Ti-alloy	0.5	C *	5		7	3.4	345
	C395W	Ti-alloy	0.5	C *	5		10.6	4.6	337
	E-Glass	Ti-alloy	0.5	B ***-20	5		1.7	1.6	409

C *: Conventional $[90/0/45/-45]_s$; A **: Conventional $[90/0]_s$; B ***: Bouligand—(angle).

Next, we look at these five concepts in detail and identify significance of parameters.

5.2. Identification of Significant Parameters

We identify significant parameters using analysis of variance (ANOVA) for parameters identified in Table 1. The condition for rejecting the null hypothesis for a linear ANOVA model is a 95% confidence interval or $P_{value} \leq 0.05$ and $F > F_{critical}$ in the F distribution table [70]. The identified significant parameters are tabulated in Table 7 from most to least significant. The insignificant parameters in Table 8 show potential for saving weight. Significance levels for parameters can be found in Appendix A.

Table 7. Significant parameters for respective structural concepts arranged in descending order.

Steel Grillage	Aluminium Grillage	FRP	Metal–FRP	Metal–Ceramic	Metal–Ceramic–Viscoelastic
• Stiffener section modulus • Stringer section modulus • Ice Stringer • Ice Stiffener	• Ice Stringer • Plate thickness • Stringer section modulus • Stiffener section modulus	• Face material • Ply thickness	• FRP material • Metal material	• Metal material • Ceramic material • Orientation	• Projectile speed • Viscoelastic layer thickness • Orientation

Table 8. Insignificant parameters for respective structural concepts.

Steel Grillage	Aluminium Grillage	FRP	Metal–FRP	Metal–Ceramic	Metal–Ceramic–Viscoelastic
• Plate thickness • Stringer spacing • Stiffener spacing	• Ice stiffener • Stringer spacing • Stiffener spacing	• Ply angle	• Metal thickness • Ply orientation	• Thickness • Thickness ratio	• Thickness ratio—ceramic/metal

5.2.1. Metal Grillage

The significant parameters between steel and aluminium grillage vary because of a difference in stiffness, as noted in literature studies [48]. For steel: the stiffener and stringer section moduli and the presence of an ice stringer and ice stiffener are significant (see Table A1). For an aluminium alloy: plate thickness, stiffener and stringer section modulus and the presence of an ice stringer are significant (see Table A2). For steel, the impact is largely carried by the ice stringer which reduces the role of plate thickness within the parametric range. Insignificance with respect to stiffener and stringer spacing indicate that impact is largely a local phenomenon. This implies a weight saving potential by reducing scantlings away from the impact region. For the more flexible aluminium alloy, the plate thickness influences structural response, which is more global than for steel.

5.2.2. FRP Composites

There is no significant difference observed between conventional and Bouligand ply arrangements. Both concepts have the same significant parameters: ply thickness, face material and impactor speed, as seen in Table A3. The relative ply angles were found to have no statistical significance on strength. For conventional ply arrangement, there is a significant difference between carbon fibre and glass fibre (p-value~2×10^{-7}), whereas for Bouligand arrangements, the p value is ~0.0012. This shows that glass fibre's suitability is improved when used in a Bouligand arrangement. This is a consequence of the helical arrangement of plies that causes it to behave like a loaded spring, resulting in a better distribution of stresses. We observe that material stiffness influences the Bouligand arrangement more. For example, the difference in carbon fibres C230UD and C395UD is more significant with the Bouligand arrangement (p-value~0.003 as opposed to ~0.02 for conventional). Additionally, the difference between UD and woven fibres shows a significant difference for Bouligand composites (p-value~2.5×10^{-8}) and insignificance for conventional composites (p-value~0.051).

5.2.3. Metal–FRP Composite

The significant parameters for this concept are respective metal and FRP materials (see Table A4). The metal has no influence on the FRP layer's SSF, while the FRP has no influence on the metal layer's SSF. Since little structural interaction between layers is observed, the layers may be designed independently. As metal thickness has no statistical significance, one can opt for smaller thicknesses to save weight. Both conventional and Bouligand arrangements performed very similarly. Among fibre types, it can be observed that woven fibres performed significantly better than UD fibres.

5.2.4. Metal–Ceramic Composite

For this composite, two orientations were investigated—(a) a ceramic layer followed by a metal layer; and (b) a metal layer followed by a ceramic layer. The significant parameters are identified as: orientation, ceramic and metal materials (Table A5). Only the ceramic's SSF is influenced by the orientation. Under the first orientation, the metal material influences the ceramic's SSF, while under the second orientation, the metal material has no significant influence. The first orientation showed 20% lower von Mises (v-m) stresses on the metal, making it more favourable option. The ceramic's SSF is influenced by the ceramic material for both orientations. BC showed 50% higher v-m stresses than SiC due to a higher impact strength. The composite thickness has no significance, implying the failure mechanism of ceramics is independent of its thickness, as expected in brittle failures. Further, the thickness ratios of respective materials have no statistical significance. A combination of SiC and aluminium results in the lowest stresses.

5.2.5. Rubber-Metal-Ceramic Composite

The addition of a viscoelastic layer to the metal–ceramic composite showed a significant improvement in the structural performance. We studied two orientations in the parametric study: (a) the viscoelastic layer between ceramic and metal; and (b) the viscoelastic layer in front of ceramic and metal. A difference between the orientations was observed to depend on the impact speed (Table A6). At 6 knots, the orientation had no significant influence, while at 10 knots the first orientation had, on average, a 50% higher ceramic and metal SSF. Another significant parameter is the viscoelastic layer thickness. The v-m stresses on the ceramic were found to decrease with increasing viscoelastic thickness. A high thickness ratio of ceramic layer:viscoelastic layer favoured the ceramic, while a low ratio favoured the metal. From a shielding perspective, the latter arrangement is beneficial.

5.3. Parametric Trends

5.3.1. Metal Grillage

There is a significant difference between the response of structural steel and aluminium alloy grillages. For steel, as the local strength in the impact region increases, the impact stress decreases. This makes the interaction a local phenomenon. For Aluminium, as the local stiffness increases, the impact stress increases. In comparison with steel, the aluminium grillage response is more global. This implies, the side girders play a role in the impact resilience as compared to steel. The dependence on side girders decreases as the central girder's section modulus is increased. Thus, we can see that material stiffness influences the impact scope in being a local or global phenomenon.

A significant interaction is observed between stiffener spacing, stringer spacing and stringer section modulus, deduced using a 2-factorial design of experiment method. In the case with a stiffener spacing 0.25 m, the aluminium grillage is very stiff and over a stringer section modulus of 303 cm^3, it starts behaving like the steel grillage and an increase in impact stress is observed for higher section moduli. Correspondingly, care must be taken in choosing the appropriate stiffener–stringer arrangement. Figure 9 shows the overall parametric influence of significant factors for metal grillages.

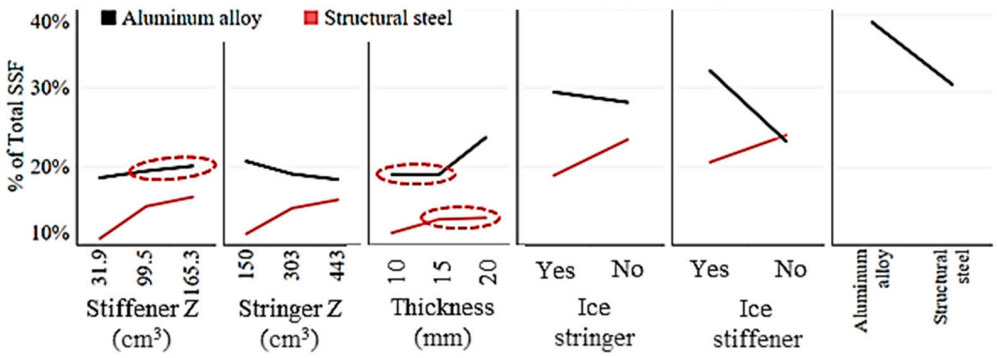

Figure 9. Parametric trends for the Steel and aluminium metal grillage. Red ellipses indicate insignificant parametric variations and represent potential areas for reducing mass.

5.3.2. FRP Composites

There is no significant difference in overall strength between Bouligand and conventional FRPs. However, the two orientations behave differently under impact, as noted in the previous section. At an impact speed of 6 knots, the *SpW* of the 20° Bouligand composite is marginally better than $|90/0/45/-45|_s$. However, at 10 knots, the observation reverses. From Figure 10, ply thickness influences the *SSF* positively but the *SpW* value decreases with ply thickness, indicating a strength-gain/mass ratio < 1. An exception to this is E-glass, which gains in *SpW*. The carbon fibre alternatives are 20–30% lighter than E-glass fibre but 2–4 times stronger than the latter, also observed in the literature [24].

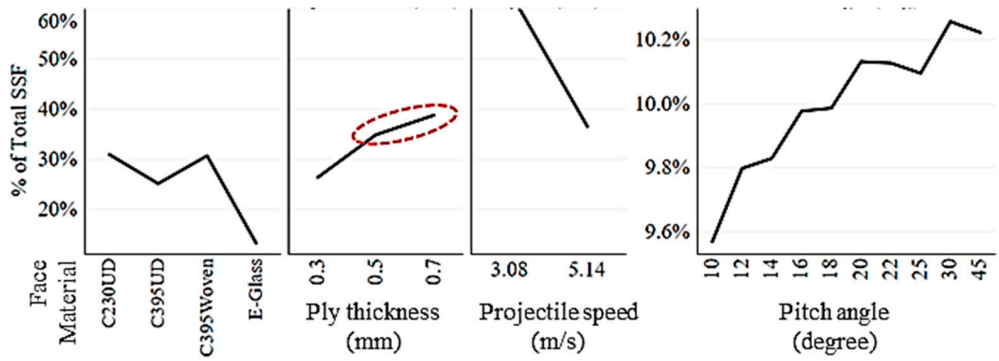

Figure 10. Parametric trends for Bouligand composite. Red ellipse indicates insignificant range.

The pitch angle influences the stress capacity positively for the Bouligand composite. Beyond 45 degrees a loss in performance is observed. Energy absorption trends indicate high energy absorption rates (>88%) for low pitch angles up to 14 degrees. An exception is the E-glass composite, which reflects the most impactor energy (>20%). The parametric trends for the conventional FRP follow similar trends (see Figure 11).

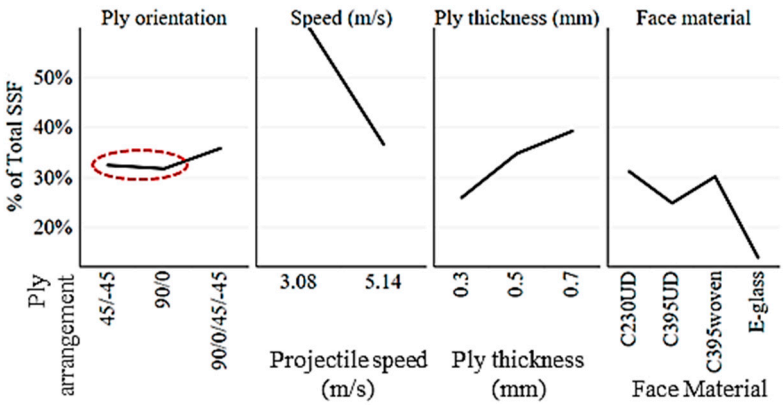

Figure 11. Parametric trends for conventional composite. Red ellipse indicates insignificant range.

5.3.3. Metal–FRP Composite

There is an evident increase in the *SSF* after the addition of a metal layer, but the addition of mass decreases the *SpW* in comparison. Among metals, titanium alloy develops nearly 40% lower peak stresses than structural steel (see Figure 12). A comparison of *SpW* (~6 times higher) clearly positions titanium alloy as the more suitable. We observe that the FRP composites are very well shielded when placed behind a rigid material. Among FRP materials, C395 woven fabric is a good choice for its light weight and ability to distribute stresses. However, using E-glass might be more practical in terms of economy and greater flexibility that provides a cushion for shock absorption on the metal cover.

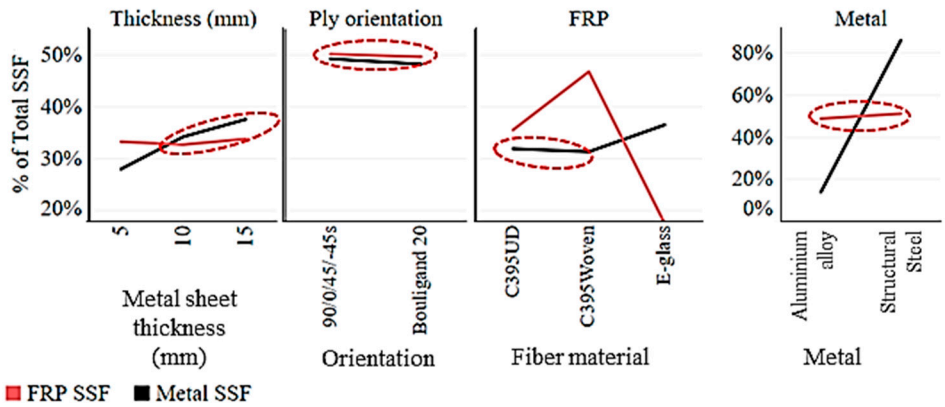

Figure 12. Parametric trends of significant factors for the Metal–FRP composite. Red ellipses indicate insignificant parametric variations.

5.4. Refined Impact Model Results

A study by Cheemakurthy and Barsoum [4] established the need for an ice stringer in metal grillages for bearing quasi-static ice pressure loads. Furthermore, we experimentally validated an aluminium grillage's response against the CZM ice model in Figure 6b. Correspondingly, we use this model to simulate impact against the lightest aluminium grillage alternative with an ice stringer for an impact speed of 6 knots.

The impact force is measured on the aluminium panel as well as the interacting ice surface. On first contact, the ice tip behaves in a ductile manner, as indicated by the first peak in Figure 13b, with a force of 42.4 kN. As the pressure increases, crushing is initiated.

The point just before the initiation of the large cracks marks the second peak with a force of 31.4 kN. Thereafter, we observe a drop in force that fluctuates due to ice spalling. The evolution of contact pressure at the impact area is shown in Figure 13c. The observed peak is ~70 MPa, which corresponds with the peak impact pressure observed in the simplified impact model.

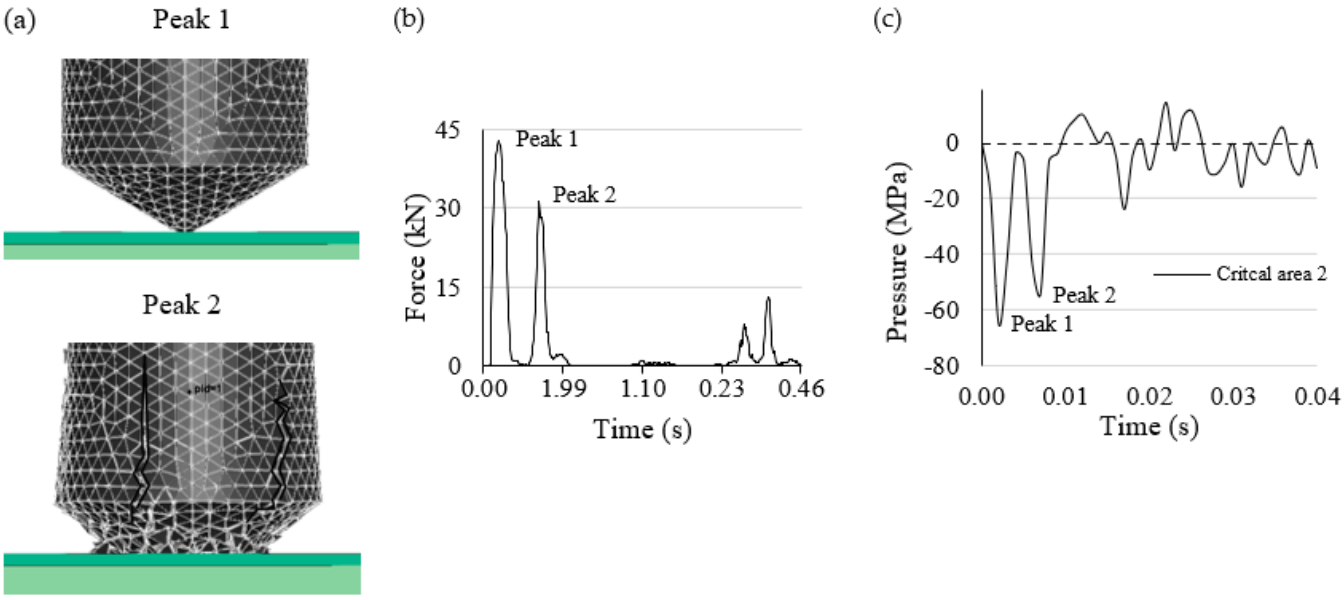

Figure 13. We observe the first peak at initial impact. The second peak is observed just before the initiation of large cracks. (**a**) Ice model behaviour, (**b**) impact forces, (**c**) impact pressures.

During impact at 6 knots, the aluminium panel oscillates with a maximum deformation of 1.6 mm as shown in Figure 14a. This compares with a deformation of 1.5 mm with the simplified impact model. The v-m stress in the impact region has a peak of 227 MPa at initial contact and 139 MPa during the initiation of large cracks (Figure 14b). The results are not in agreement with the simplified impact model which predicts a stress of 98 MPa. The difference can be attributed to a difference in impactor shape, a ~6 time difference in impactor mass and material model.

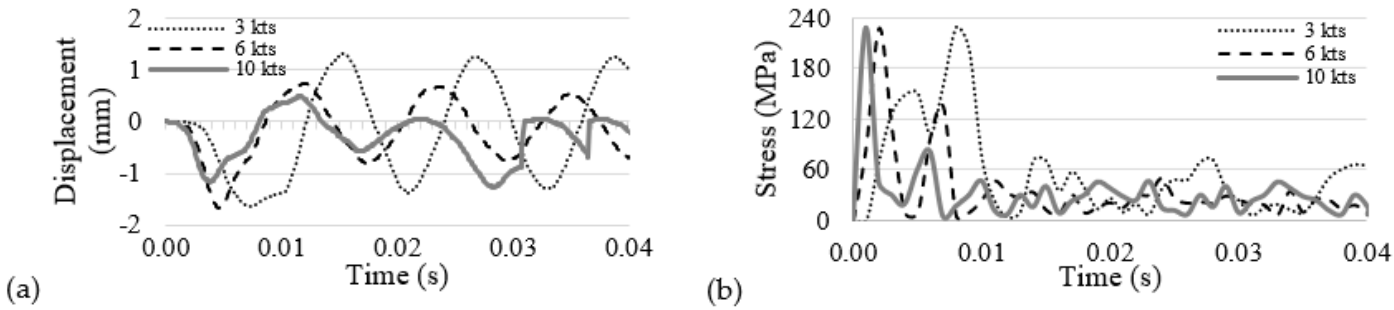

Figure 14. (**a**) Deformation, (**b**) stresses on the aluminium panel after impact with ice at speeds: 3, 6 and 10 knots.

Parametric Exploration

Three impact speeds are investigated: 3, 6 and 10 knots. From Figure 15, the impact force duration is inversely proportional to the impactor speed. The initial impact magnitude increases logarithmically from 26.7 kN to 51.2 kN. On the other hand, the secondary force caused by crushing decreases from 37.9 kN to 19.4 kN. This implies that it is not necessarily

safer to operate at a lower speed. However, the force duration is larger at slower speeds, allowing the utilisation of concepts like sandwich structures.

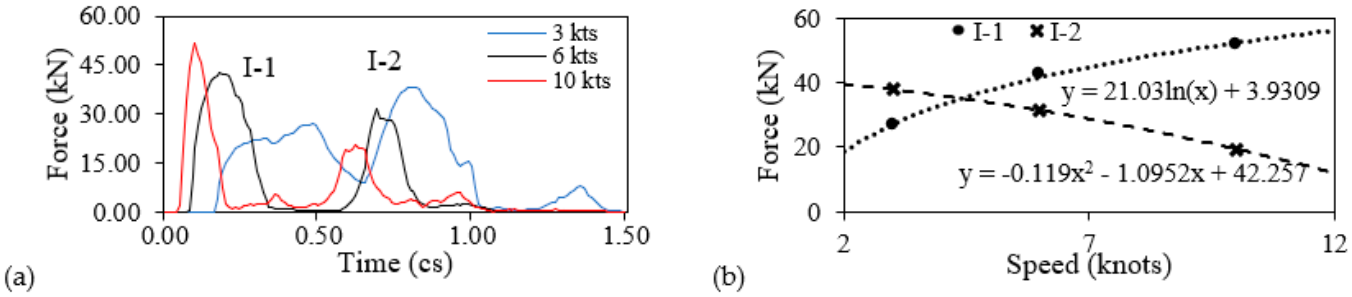

Figure 15. Forces in contact region at different impact speeds. (**a**) Force time distribution. (**b**) Force speed distribution.

A comparison of contact pressures in Figure 16 indicates that at higher speeds, the peak magnitudes decrease. This could be due to the very short interaction time or a result of high impact energy causing the easier crushing of ice.

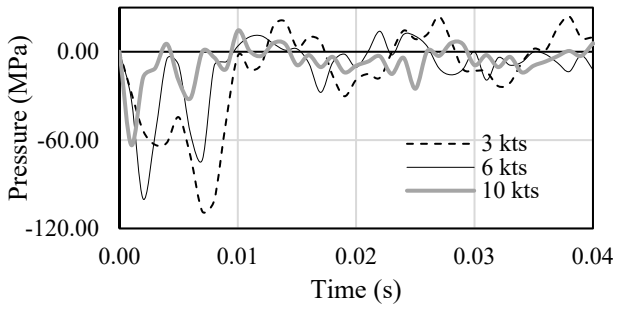

Figure 16. Comparison of peak pressures at different impact speeds.

A comparison of deformations in Figure 14a shows that deformation magnitudes decreases while the oscillation frequency increases with speed. A comparison of stresses in Figure 14b shows an independence of peak stress and impact speed. The largest magnitude remained consistent at around ~230 MPa. The initial impact is larger at high speed, while secondary force is more important at low speed. From this we can conclude that structural response is more dependent on the ice properties rather than impact speed. This reinforces the need for accurate ice data.

The CZM ice impact model tests show that the aluminium grillage is a good candidate. However, it is important to note that this does not justify the ice survivability for other structural concepts. The CZM model for other structural concepts needs to be experimentally validated before conclusions on survivability can be ascertained.

6. Discussion

A parametric study of the structural response of five structural concepts and respective materials subjected to impact is carried out in the current study. Two impact models were used—(a) a rigid body impact model to study relative performance of parametrised structures and (b) an experimentally validated ice-representative CZM ice model to study the structural response of an aluminium grillage. It was noted that strength was a more critical factor than stiffness. With respect to strength, FRP composites were the most favourable in terms of strength capacity by mass (*SpW*). However, considering their susceptibility to BVID [5,18,19], punctures and delamination [69], an aluminium grillage or a metal–FRP composite are suited better.

Among FRP composites, two ply arrangements were studied—(a) Bouligand and (b) a conventional arrangement. The helical arrangement behaved like a loaded coil,

which improved the stress distribution on impact. This can be observed in Figure 17, where the impact zone has lower peak stresses in general, while stresses in the rest of the region assume a spiral distribution and a wider spread. Furthermore, the back panel has considerably lower stresses. We also note a 2–5% lower stiffness of Bouligand arrangements, which supports the loaded coil hypothesis. The arrangement responds to impact energy in a new way and presents an interesting area for further investigation against ice impacts.

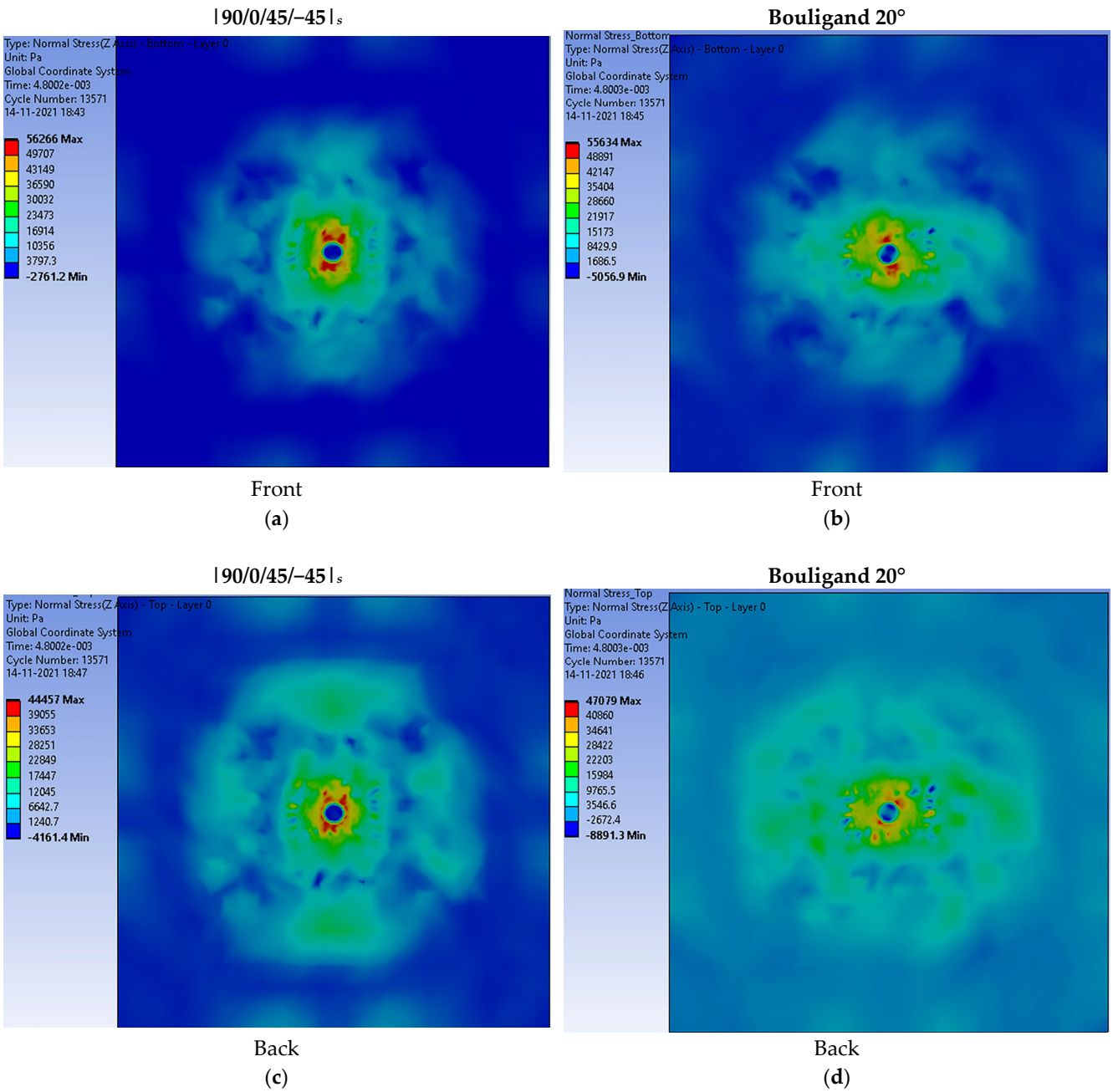

Figure 17. Stress distribution on the front (**a**,**b**) and back (**c**,**d**) faces of a conventional (**a**,**c**) and Bouligand (**b**,**d**) FRP.

An aluminium alloy metal grillage is identified as a potentially good candidate. A naturally low stiffness of the material makes it flexible, and its behaviour is unlike the naturally rigid steel [11]. Broadly, it was identified that the presence of an ice stringer increases local impact stresses. However, it is a necessary requirement for bearing quasi-static pressure loads [4]. This case was further investigated with the CZM ice impact model.

The structure shows good survivability at different ice impact speeds for an ice mass representing ice conditions in Stockholm. However, one needs to be aware that the use of larger ice masses were seen to cause plastic deformations [11,71]. In this case, a metal–FRP composite might be the way forward. For this concept, titanium alloy was the more weight and strength efficient alternative but is also more expensive and less green [37].

It should be noted that the stresses from the CZM model were higher than with a rigid body impactor because of a difference in mass, geometry and element construction. To account for this difference, the parametric range of structural concepts were chosen to be larger while studying the relative performance using the simplified model.

Some limitations of the study are:

1. The rigid body impactor's behaviour was assumed to mimic ice impact. Considering the nature of the parametric study was to ascertain relative performance, the loss in accuracy was assumed to be acceptable.
2. The division of the ice–hull interaction into three independent processes is an idealisation. In real life, the phases may overlap.
3. The CZM model was validated with experiments for an aluminium alloy structure. The same model is not valid for rigid structures. This will be explored as part of future work.
4. There was a lack of experimental validation for the simplified impact model. To overcome this limitation, the scope was limited to low-velocity impact, where the effects of high strain rates on deformable materials can be neglected. Further, by limiting our investigation to relative structural performance, we can reduce the need for accurate solutions.

Some opportunities for future work include:

1. Ice impact experimental studies on structural concepts (other than aluminium grillage) and the validation of CZM ice model for these structural concepts.
2. The exploration of fibre–metal laminates (FML); several studies have shown their effectiveness against impact loads [72,73].
3. Further exploration of the beneficial effect of adding a viscoelastic layer to other structural concepts.

The principal outcome of the study is a viable pool of alternatives suited towards impact loading. These alternatives, in combination with quasi-static pressure load candidates [4], will contribute towards the development of a lightweight ice-going ferries. Such ferries would be able to work with similar efficiency as non-ice vessels in terms of fuel efficiency, emissions and costs. For waterborne public transportation, this would result in higher customer satisfaction [74,75] and improve public transport providers' perception of WPT [76].

7. Conclusions

Five lightweight structural concepts were investigated parametrically for rule-based strength and stiffness using dynamic finite element method in LS Dyna. The following conclusions may be drawn from the study:

1. The metal–FRP composite was identified as the most suitable candidate, since it offered a high *SpW* and low mass, while protecting against structural damage and BVID. FRP candidates were the lightest suitable alternative but are susceptible to BVID. Aluminium alloy grillage was light and suitable but prone to plastic deformations that may affect resistance performance.
2. There was a significant difference in impact behaviour of rigid and flexible structures. This was observed in the difference in significant parameters for aluminium and steel grillages.
3. The Bouligand FRP ply arrangement resulted in better impact stress distribution than conventional arrangements. The back panel for Bouligand composites showed significantly lower stress.

4. The addition of a viscoelastic layer showed a significant reduction in impact stresses with the ceramic–metal composite. The concept may be extended in combination with other concepts.
5. The aluminium alloy grillage showed good survivability against the refined ice impact model for impact speeds up till 10 knots.

The study's outcomes contribute towards the development of a lightweight robust ice-going hull, leading to efficient year-round, environmentally sustainable, waterborne mobility.

Author Contributions: Conceptualization, H.C., K.G. and M.B.; methodology, H.C. and Z.B.; software, H.C.; validation, H.C. and Z.B.; formal analysis, H.C.; investigation, H.C.; resources, M.B. and K.G.; data curation, H.C. and Z.B.; writing—original draft preparation, H.C.; writing—review and editing, H.C., Z.B. and K.G.; visualization, H.C. and Z.B.; supervision, Z.B., M.B. and K.G.; project administration, K.G.; funding acquisition, K.G. All authors have read and agreed to the published version of the manuscript.

Funding: The Swedish Transport Administration is acknowledged for financially supporting the research program Waterborne Urban Mobility TRV 2018/6471.

Institutional Review Board Statement: Not applicable.

Informed Consent Statement: Not applicable.

Data Availability Statement: The data presented in this study are available on request from the corresponding author.

Acknowledgments: We are thankful to the Institute for ship structural design and analysis at Technische Universität Hamburg (TUHH) for providing assistance and experimental data on ice impact tests.

Conflicts of Interest: The authors declare no conflict of interest.

Appendix A. Significance Values of Structural Concept Parameters

Table A1. Structural steel grillage SSF: Statistically significant parameters are underlined.

Parameter	SS	MS	F	*p*-Value	F Crit	Rank
Plate thickness	1.23	0.62	1.2	0.303	3.03	
Stiffener Z	21.09	10.54	24.4	2.25×10^{-10}	3.03	1
Stringer Z	13.95	6.98	15.1	6.64×10^{-7}	3.03	2
Ice Stiffener	2.07	2.07	4.33	0.039	3.9	4
Ice Stringer	2.78	2.78	5.03	0.026	3.9	3
Stringer spacing	0.05	0.05	0.1	0.751	3.9	
Stiffener spacing	1.14	1.14	2.38	0.125	3.9	

Table A2. Aluminum alloy grillage SSF: Statistically significant parameters are underlined.

Parameter	SS	MS	F	*p*-Value	F Crit	Rank
Plate thickness	1.4×10^{16}	6.99×10^{15}	14.10	1.62×10^{-6}	3.03	2
Stiffener Z	2.182615	1.091307	4.32	0.01	3.03	4
Stringer Z	5.21×10^{15}	2.61×10^{15}	4.90	0.01	3.03	3
Ice Stiffener	1.91×10^{14}	1.91×10^{14}	0.36	0.55	3.90	
Ice Stringer	5.4×10^{16}	5.4×10^{16}	172.76	3.15×10^{-27}	3.90	1
Stringer spacing	9.07×10^{13}	9.07×10^{13}	0.58	0.45	3.90	
Stiffener spacing	2.48×10^{13}	2.48×10^{13}	0.04	0.85	3.90	

Table A3. FRP arrangement SSF. Statistically significant parameters are underlined.

Parameter	Ply Orientation	SS	MS	F	*p*-Value	F Crit	Rank
Ply angle	Conventional	1.02	0.51	0.45	0.64	3.28	
	Bouligand	0.20	0.20	0.15	0.70	4.30	
Ply thickness	Conventional	9.39	4.70	5.38	0.01	3.28	4
	Bouligand	29.60	14.80	15.00	1.58×10^{-6}	3.07	2
Face material	Conventional	20.98	10.49	31.89	1.74×10^{-7}	3.40	1
	Bouligand	17.28	8.64	7.84	7.42×10^{-4}	3.10	3

Table A4. Metal–FRP composite SSF. Statistically significant parameters are underlined.

Parameter	SSF Region	SS	MS	F	*p*-Value	F Crit	Rank
Metal thickness	FRP	0.06	0.03	0.02	0.98	3.28	
	Metal	212.13	106.06	0.43	0.65	3.28	
FRP material	FRP	46.90	23.45	1756.49	3.05×10^{-34}	3.28	1
	Metal	72.63	36.32	0.15	0.86	3.28	
Metal material	FRP	0.20	0.20	0.14	0.71	4.13	
	Metal	7812.54	7812.54	593.10	4.21×10^{-23}	4.13	2
Ply orientation	FRP	0.01	0.01	0.01	0.94	4.13	
	Metal	1.06	1.06	0.00	0.95	4.13	

Table A5. Metal–Ceramic composite SSF. Statistically significant parameters are underlined.

Parameter	Region	Orientation	SS	MS	F	*p*-Value	F Crit	Rank
Thickness			0.01	0.003	1.30	0.28	2.69	
Orientation	Metal		0.40	0.40	0.15	0.70	3.93	
	Ceramic		0.03	0.03	12.87	0.0005	3.93	5
Thickness ratio	Metal	CERA-MET	1.53	0.38	0.13	0.97	2.55	
	Ceramic	CERA-MET	0.00	0.0006	0.68	0.61	2.53	
	Metal	MET-CERA	1.02	0.26	0.10	0.98	1.02	
	Ceramic	MET-CERA	0.003	0.0008	0.19	0.94	2.55	
Ceramic material	Ceramic	CERA-MET	0.01	0.01	20.95	2.81×10^{-5}	4.02	4
	Ceramic	MET-CERA	0.19	0.19	298.40	7.04×10^{-24}	4.02	3
	Metal	CERA-MET	0.59	0.59	0.24	0.63	4.02	
	Metal	MET-CERA	0.39	0.39	0.14	0.71	4.02	
Metal material	Ceramic	CERA-MET	0.01	0.01	10.79	0.001796	4.02	6
	Ceramic	MET-CERA	0.00	0.0004	0.11	0.74	4.02	
	Metal	CERA-MET	135.45	135.45	458.51	4.67×10^{-28}	4.02	2
	Metal	MET-CERA	126.78	126.78	596.70	3.33×10^{-31}	4.02	1

Table A6. Metal–Viscoelastic–Ceramic SSF. Statistically significant parameters are underlined.

Parameter	SSF Region	SS	MS	F	*p*-Value	F Crit	Rank
Orientation	Ceramic	0.05	0.05	3.76	0.06	4.10	
	Metal	0.18	0.18	4.55	0.04	4.10	5
Viscoelastic layer thickness	Ceramic	0.08	0.08	5.80	0.02	4.10	3
	Metal	0.18	0.18	4.60	0.04	4.10	4
Impactor speed	Ceramic	0.13	0.13	10.55	0.002428	4.10	2
	Metal	0.75	0.75	31.01	2.23×10^{-6}	4.10	1
Thickness ratio Ceramic: metal	Ceramic	0.02	0.00	0.30	0.88	2.64	
	Metal	0.28	0.07	1.75	0.16	2.64	

References

1. FSICR. *Finnish Swedish Ice Class Rules*; Contract No.: TRAFI/708629/03.04.01.01/2018; Finnish Transport and Communication Agency Traficom: Helsinki, Finland, 2017.
2. DNVGL. *Rules for Classification—Ships*; Part 6 Additional Class Notations: Chapter 6 Cold Climate; DNV GL: Bærum, Norway, 2015.
3. IACS. *UR I2 Structural Requirements for Polar Class Ships*; Contract No.: UR I2 Rev4 CLN; IACS: London, UK, 2019.
4. Cheemakurthy, H.; Barsoum, Z.; Burman, M.; Garme, K. Lightweight Structural Concepts in Bearing Quasi-Static Ice Hull Interaction Loads. *J. Mar. Sci. Eng.* **2022**, *10*, 416. [CrossRef]
5. Davies, G.; Olsson, R. Impact on composite structures. *Aeronaut. J.* **2004**, *108*, 541–563. [CrossRef]
6. Bogenfeld, R.; Kreikemeier, J.; Wille, T. Review and benchmark study on the analysis of low-velocity impact on composite laminates. *Eng. Fail. Anal.* **2018**, *86*, 72–99. [CrossRef]
7. Timco, G.W.; Frederking, R.M.W. An investigation of the failure envelope of granular/discontinuous-columnar sea ice. *Cold Reg. Sci. Technol.* **1984**, *9*, 17–27. [CrossRef]
8. Kim, H.; Daley, C.; Kim, H. Evaluation of large structural grillages subjected to ice loads in experimental and numerical analysis. *Mar. Struct.* **2018**, *61*, 467–502. [CrossRef]
9. Prato, A.; Longana, M.L. A novel approach for the investigation of low energy ice impacts. *Int. J. Impact Eng.* **2018**, *121*, 12–19. [CrossRef]
10. Banik, A.; Zhang, C.; Khan, M.; Wilson, M.; Tan, K. Low-Velocity Ice Impact Response and Damage Phenomena on Steel and CFRP Sandwich Composite. *Int. J. Impact Eng.* **2021**, *162*, 104134. [CrossRef]
11. Herrnring, H.; Kubiczek, J.M.; Ehlers, S.; Niclasen, N.O.; Burmann, M. Experimental investigation of an accidental ice impact on an aluminium high speed craft. In *Progress in the Analysis and Design of Marine Structures*; CRC Press: Boca Raton, FL, USA, 2017; pp. 697–704.
12. Kujala, P.; Goerlandt, F.; Way, B.; Smith, D.; Yang, M.; Khan, F.; Veitch, B. Review of risk-based design for ice-class ships. *Mar. struct.* **2019**, *63*, 181–195. [CrossRef]
13. Cheemakurthy, H.; Zhang, M.; Garme, K.; Burman, M.; Ehlers, S.; von Bock und Polach, R. (Eds.) Statistical estimation of uncertainties associated with ship operations in fresh water ice. In Proceedings of the 28th International Ocean and Polar Engineering Conference, Sapporo, Japan, 10–15 June 2018.
14. Burman, M.; Niclasen, N. *Ice Impact on Sandwich Panels for Light Weight Marine Vessels*; Florida Atlantic University: Fort Lauderdale, FL, USA, 2016.
15. Crum, K.A.; McMichael, J.; Novak, M. (Eds.) Advances in aluminum relative to ship survivability. In Proceedings of the American Society of Naval Engineers Day 2012 Conference, Arlington, VA, USA, 9–10 February 2012.
16. Wu, X.; Li, Y.; Cai, W.; Guo, K.; Zhu, L. Dynamic responses and energy absorption of sandwich panel with aluminium honeycomb core under ice wedge impact. *Int. J. Impact Eng.* **2021**, *162*, 104137. [CrossRef]
17. Niclasen, N.O. *Light Weight Marine Vessels Operating in Brash Ice*; KTH: Stockholm, Sweden, 2015.
18. Zhang, C.; Tan, K. Low-velocity impact response and compression after impact behavior of tubular composite sandwich structures. *Compos. Part B Eng.* **2020**, *193*, 108026. [CrossRef]
19. Cantwell, W.J.; Morton, J. The impact resistance of composite materials—A review. *Composites* **1991**, *22*, 347–362. [CrossRef]
20. Yoon, S.-H.; Park, S. A mechanical analysis of woodpecker drumming and its application to shock-absorbing systems. *Bioinspir. Biomim.* **2011**, *6*, 016003. [CrossRef] [PubMed]
21. Drake, A.; Donahue, T.L.H.; Stansloski, M.; Fox, K.; Wheatley, B.B.; Donahue, S.W. Horn and horn core trabecular bone of bighorn sheep rams absorbs impact energy and reduces brain cavity accelerations during high impact ramming of the skull. *Acta Biomater.* **2016**, *44*, 41–50. [CrossRef] [PubMed]
22. Guarín-Zapata, N.; Gomez, J.; Yaraghi, N.; Kisailus, D.; Zavattieri, P.D. Shear wave filtering in naturally-occurring Bouligand structures. *Acta Biomater.* **2015**, *23*, 11–20. [CrossRef] [PubMed]
23. Sun, J.; Liu, C.; Bhushan, B. A review of beetle hindwings: Structure, mechanical properties, mechanism and bioinspiration. *J. Mech. Behav. Biomed. Mater.* **2019**, *94*, 63–73. [CrossRef] [PubMed]
24. Håkansson, M.; Johnson, E.; Ringsberg, J.W. Cost and weight of composite ship structures: A parametric study based on Det Norske Veritas rules. *Proc. Inst. Mech Eng. Part M J. Eng. Marit Environ.* **2018**, *232*, 331–350. [CrossRef]
25. Wang, J.; Waas, A.M.; Wang, H. Experimental and numerical study on the low-velocity impact behavior of foam-core sandwich panels. *Compos. Struct.* **2013**, *96*, 298–311. [CrossRef]
26. Maneepan, K. *Genetic Algorithm Based Optimisation of FRP Composite Plates in Ship Structures*; University of Southampton: Southampton, UK, 2007.
27. Kellner, L.; Stender, M.; Herrnring, H.; Ehlers, S.; Hoffmann, N.; Høyland, K.V. Establishing a common database of ice experiments and using machine learning to understand and predict ice behavior. *Cold Reg. Sci. Technol.* **2019**, *162*, 56–73. [CrossRef]
28. Jordaan, I.J. Mechanics of ice–structure interaction. *Eng. Fract. Mech.* **2001**, *68*, 1923–1960. [CrossRef]
29. Mouritz, A.P.; Gellert, E.; Burchill, P.; Challis, K. Review of advanced composite structures for naval ships and submarines. *Compos. Struct.* **2001**, *53*, 21–42. [CrossRef]
30. Zhao, X.-L. *FRP-Strengthened Metallic Structures*; CRC Press: Boca Raton, FL, USA, 2013; ISBN 0203895215.

31. Rubino, F.; Nisticò, A.; Tucci, F.; Carlone, P. Marine application of fiber reinforced composites: A review. *J. Mar. Sci. Eng.* **2020**, *8*, 26. [CrossRef]
32. Momčilović, N.; Motok, M. Estimation of ship lightweight reduction by means of application of sandwich plate system. *FME Trans.* **2009**, *37*, 123–128.
33. DNVGL. *Rules for Classification: Inland Navigation Vessels (RU-INV)*; DNV GL: Bærum, Norway, 2017.
34. Ouyang, W.; Gong, B.; Wang, H.; Scarpa, F.; Su, B.; Peng, H.-X. Identifying optimal rotating pitch angles in composites with Bouligand structure. *Compos. Commun.* **2021**, *23*, 100602. [CrossRef]
35. Ghiasi, H.; Pasini, D.; Lessard, L. Optimum stacking sequence design of composite materials Part I: Constant stiffness design. *Compos Struct.* **2009**, *90*, 1–11. [CrossRef]
36. Chiandussi, G.; Fontana, R.; Urbinati, F. Design sensitivity analysis method for multidisciplinary shape optimisation problems with linear and non-linear responses. *Eng. Comput.* **1998**, *15*, 391–417. [CrossRef]
37. ANSYS. *Material Database: Ansys Granta EduPack Software*; Version 2020R2; ANSYS Inc.: Cambridge, UK, 2021.
38. Steinberg, D. *Equation of State and Strength Properties of Selected Materials*; Lawrence Livermore National Laboratory: Livermore, CA, USA, 1996.
39. Westerling, L.; Lundberg, P.; Lundberg, B. Tungsten long-rod penetration into confined cylinders of boron carbide at and above ordnance velocities. *Int. J. Impact Eng.* **2001**, *25*, 703–714. [CrossRef]
40. Treloar, L. Stress-strain data for vulcanized rubber under various types of deformation. *Rubber Chem. Technol.* **1944**, *17*, 813–825. [CrossRef]
41. Timco, G.; Weeks, W. A review of the engineering properties of sea ice. *Cold Reg. Sci. Technol.* **2010**, *60*, 107–129. [CrossRef]
42. Idrissova, S.; Bergström, M.; Hirdaris, S.E.; Kujala, P. Analysis of a collision-energy-based method for the prediction of Ice loading on ships. *Appl. Sci.* **2019**, *9*, 4546. [CrossRef]
43. Cheemakurthy, H.; Zhang, M.; Garme, K.; Barsoum, Z. (Eds.) Nonlinear Finite Element Analysis of Inland-Waterway Barge in Fresh Water Ice Conditions. In Proceedings of the 29th International Ocean and Polar Engineering Conference, Honolulu, HI, USA, 16–21 June 2019.
44. Zhang, M.; Cheemakurthy, H.; Ehlers, S.; Franz von Bock und Polach, R.; Garme, K.; Burman, M. Ice pressure prediction based on the probabilistic method for ice-going vessels in inland waterways. *J. Offshore Mech. Arct. Eng.* **2019**, *141*, 021501. [CrossRef]
45. Gürtner, A. Experimental and Numerical Investigations of Ice-Structure Interaction. Ph.D. Thesis, Norwegian University of Science and Technology, Trondheim, Norway, 2009.
46. Kuutti, J.; Kolari, K.; Marjavaara, P. Simulation of ice crushing experiments with cohesive surface methodology. *Cold Reg. Sci. Technol.* **2013**, *92*, 17–28. [CrossRef]
47. Daiyan, H.; Sand, B. (Eds.) Numerical simulation of the ice-structure interaction in LS-DYNA. In Proceedings of the 8th European LSDYNA Users Conference, Strasbourg, France, 23–24 May 2011.
48. Herrnring, H.; Kellner, L.; Kubiczek, J.M.; Ehlers, S. (Eds.) Simulation of Ice-Structure Interaction with CZM-Elements. In Proceedings of the 18th German LS-Dyna Forum, Bamberg, Germany, 15–17 October 2018.
49. Dávila, C.G.; Camanho, P.P. Decohesion elements using two and three-parameter mixed-mode criteria. In Proceedings of the American Helicopter Society Conference, Williamsburg, VA, USA, 1 January 2001.
50. Tabiei, A.; Zhang, W. Cohesive element approach for dynamic crack propagation: Artificial compliance and mesh dependency. *Eng. Fract Mech.* **2017**, *180*, 23–42. [CrossRef]
51. Falk, M.L.; Needleman, A.; Rice, J.R. A critical evaluation of cohesive zone models of dynamic fractur. *J. Phys. IV* **2001**, *11*, Pr5-43–Pr5-50. [CrossRef]
52. FSICR. *Finnish Swedish Ice Class Rules*; Contract No.: TRAFI/31298/03.04.01.00/2010; Finnish Transport and Communication Agency Traficom: Helsinki, Finland, 2010.
53. Li, F.; Kotilainen, M.; Goerlandt, F.; Kujala, P. An extended ice failure model to improve the fidelity of icebreaking pattern in numerical simulation of ship performance in level ice. *Ocean Eng.* **2019**, *176*, 169–183. [CrossRef]
54. Lindquist, A. Straightforward method for calculation of ice resistance of ships. *POAC* **1989**, *2*, 722.
55. DNVGL. *Rules for Classification—Ships*; Part 3 Hull, Chapter 4 Loads; DNV GL: Bærum, Norway, 2017.
56. Ivañez, I.; Sanchez-Saez, S. Numerical modelling of the low-velocity impact response of composite sandwich beams with honeycomb core. *Compos. Struct.* **2013**, *106*, 716–723. [CrossRef]
57. Wade, B.; Feraboli, P.; Osborne, M. *Simulating Laminated Composites Using LS-DYNA Material Model MAT54 Part I: [0] and [90] Ply Single-Element Investigation*; FAA JAMS: Baltimore, MD, USA, 2012.
58. Bao, J.; Wang, Y.; An, R.; Zhang, B.; Cheng, H.; Wang, F. The Effect of Interlayer Materials on Ceramic Damage in SiC/Al Composite Structure. *Materials* **2020**, *13*, 3709. [CrossRef]
59. Forquin, P.; Tran, L.; Louvigné, P.-F.; Rota, L.; Hild, F. Effect of aluminum reinforcement on the dynamic fragmentation of SiC ceramics. *Int. J. Impact Eng.* **2003**, *28*, 1061–1076. [CrossRef]
60. Chi, R.; Serjouei, A.; Sridhar, I.; Geoffrey, T.E. Pre-stress effect on confined ceramic armor ballistic performance. *Int. J. Impact Eng.* **2015**, *84*, 159–170. [CrossRef]
61. Kim, B.; Lee, S.B.; Lee, J.; Cho, S.; Park, H.; Yeom, S.; Sung, H.P. A comparison among Neo-Hookean model, Mooney-Rivlin model, and Ogden model for chloroprene rubber. *Int. J. Precis. Eng. Manuf.* **2012**, *13*, 759–764. [CrossRef]

62. Albayrak, M.; Kaman, M.O. (Eds.) Low Velocity Impact Behavior of Aluminum Sandwich Plates Having Rubber Core. In Proceedings of the International Conference on Material Science and Technology in Kazilcahamam, Kazilcahamam, Ankara, Turkey, 18–20 October 2019.
63. Sevkat, E.; Liaw, B.; Delale, F. Drop-weight impact response of hybrid composites impacted by impactor of various geometries. *Mater. Des.* **2013**, *52*, 67–77. [CrossRef]
64. Beaumont, P.W.R. *Fracture Mechanisms in Fibrous Composites*; Fracture Mechanics; Elsevier: Amsterdam, The Netherlands, 1979; pp. 211–233. [CrossRef]
65. Hashin, Z. Failure criteria for unidirectional fiber composites. *J. Appl. Mech.* **1980**, *47*, 329–334. [CrossRef]
66. Rajendran, A.; Kroupa, J. Impact damage model for ceramic materials. *J. Appl. Phys.* **1989**, *66*, 3560–3565. [CrossRef]
67. Taylor, L.; Chen, E.P.; Kuszmaul, J.S. Microcrack-induced damage accumulation in brittle rock under dynamic loading. *Comp. Meth. Appl. Mech. Eng.* **1986**, *55*, 301. [CrossRef]
68. Budiansky, B.; O'connell, R.J. Elastic moduli of a cracked solid. *Int. J. Solids Struct.* **1976**, *12*, 81–97. [CrossRef]
69. Liu, D.; Raju, B.B.; Dang, X. Size effects on impact response of composite laminates. *Int. J. Impact Eng.* **1998**, *21*, 837–854. [CrossRef]
70. Taguchi, G.; Elsayed, E.A.; Hsiang, T.C. *Quality Engineering in Production Systems*; McGraw-Hill College: New York City, NY, USA, 1989.
71. Smerd, R.; Winkler, S.; Salisbury, C.; Worswick, M.; Lloyd, D.; Finn, M. High strain rate tensile testing of automotive aluminum alloy sheet. *Int. J. Impact Eng.* **2005**, *32*, 541–560. [CrossRef]
72. He, W.; Wang, L.; Liu, H.; Wang, C.; Yao, L.; Li, Q.; Sun, G. On impact behavior of fiber metal laminate (FML) structures: A state-of-the-art review. *Thin-Walled Struct.* **2021**, *167*, 108026. [CrossRef]
73. Sadighi, M.; Alderliesten, R.; Benedictus, R. Impact resistance of fiber-metal laminates: A review. *Int. J. Impact Eng.* **2012**, *49*, 77–90. [CrossRef]
74. Tanko, M.; Cheemakurthy, H.; Kihl, S.H.; Garme, K. Water transit passenger perceptions and planning factors: A Swedish perspective. *Travel Behav. Soc.* **2019**, *16*, 23–30. [CrossRef]
75. Cheemakurthy, H.; Tanko, M.; Garme, K. *Urban Waterborne Public Transport Systems: An Overview of Existing Operations in World Cities*; Contract No.: 1651-7660; KTH Royal Institute of Technology: Stockholm, Sweden, 2018; ISBN 978-91-7729-648-5. [CrossRef]
76. Cheemakurthy, H.; Garme, K. A modularly tailored commuter ferry platform. *Int. Shipbuild. Prog.* **2022**, 1–35, *Pre-Press*. [CrossRef]